

Weak Lensing Reconstruction by Counting DECaLS Galaxies

Jian Qin^{1,2,*} Pengjie Zhang^{1,3,2,†} Haojie Xu^{4,1,2} Yu Yu^{1,2,‡} Ji Yao^{4,1,2} Ruijie Ma^{1,2} and Huanyuan Shan⁴

¹*Department of Astronomy, School of Physics and Astronomy,
Shanghai Jiao Tong University, Shanghai, 200240, China*

²*Key Laboratory for Particle Astrophysics and Cosmology (MOE)/Shanghai
Key Laboratory for Particle Physics and Cosmology, China*

³*Tsung-Dao Lee Institute, Shanghai Jiao Tong University, Shanghai, 200240, China*

⁴*Shanghai Astronomical Observatory, Chinese Academy of Sciences, Shanghai 200030, China*

Abstract

Alternative to weak lensing measurements through cosmic shear, we present a weak lensing convergence $\hat{\kappa}$ map reconstructed through cosmic magnification effect in DECaLS galaxies of the DESI imaging surveys DR9. This is achieved by linearly weighing 12 maps of galaxy number overdensity in different magnitude bins of grz photometry bands. The weight is designed to eliminate the mean galaxy deterministic bias, minimize galaxy shot noise while maintaining the lensing convergence signal. We also perform corrections of imaging systematics in the galaxy number overdensity. The $\hat{\kappa}$ map has 8365 deg² sky coverage. Given the low number density of DECaLS galaxies, the $\hat{\kappa}$ map is overwhelmed by shot noise and the map quality is difficult to evaluate using the lensing auto-correlation. Alternatively, we measure its cross-correlation with the cosmic shear catalogs of DECaLS galaxies of DESI imaging surveys DR8, which has 8365 deg² overlap in sky coverage with the $\hat{\kappa}$ map. We detect a convergence-shear cross-correlation signal with $S/N \approx 10$. The analysis also shows that the galaxy intrinsic clustering is suppressed by a factor $O(10^2)$ and the residual galaxy clustering contamination in the $\hat{\kappa}$ map is consistent with zero. Various tests with different galaxy and shear samples, and the Akaike information criterion analysis all support the lensing detection. So is the imaging systematics corrections, which enhance the lensing signal detection by $\sim 30\%$. We discuss various issues for further improvement of the measurements.

I. INTRODUCTION

Weak lensing, which probe directly the matter distribution of the Universe, provide powerful insight into dark energy, dark matter and gravity at cosmological scales [1–7]. An effect of weak lensing is cosmic shear, which distorts shapes of distant galaxies. This signal can be extracted statistically from the galaxy images and has been the main target of current weak lensing studies. With large surveys, such as the on-going Dark Energy Survey [DES, 8], the Kilo-Degree Survey [KiDS, 9], and the Hyper Suprime-Cam Subaru Strategic Program survey [HSC-SSP, 10], cosmic shear contributed significantly to the precision cosmology [e.g., 11–17].

Another weak lensing effect is cosmic magnification, which induces changes in the observed galaxy number density by magnifying the galaxy flux and resizing the solid angle of the sky patches [18, 19]. As the galaxy intrinsic alignment contaminates the cosmic shear signal, the galaxy intrinsic clustering contaminates the cosmic magnification signal. In observations, cosmic magnification is typically measured through cross correlations of two samples in the same patch of the sky but widely separated in redshift. Lenses include luminous red galaxies (LRGs) and clusters [e.g., 20–23]. Sources at higher redshifts include quasars [24, 25], Lyman break galaxies [26, 27], and submillimetre galaxies [28, 29]. In addition to this, the magnification effects can be detected through the shift in number count, magnitude and size [30–35]. Recently, cross-correlation between cosmic magnification and cosmic shear has been detected in HSC [36] and DECaLS \times DESI [37].

Instead of the indirect measurements of cosmic magnification through cross-correlation, it is in principle possible to extract the magnification signal directly from multiple galaxy overdensity maps of different brightness [38–44]. The key information to use here is the characteristic flux dependence of magnification bias. The major contamination to eliminate is the intrinsic galaxy clustering. The galaxy bias is complicated [e.g. 45–47], however the leading order component to eliminate is the deterministic bias. [44] proposed a modified internal linear combination (ILC) method, which can eliminate the average galaxy bias model-independently.

We extend the methodology of [44] to utilize multiple photometry band information. Including the multi-band information not only improves the mitigation of galaxy intrinsic clustering, but also suppresses shot noise, as recently shown by [48]. We then apply it to DECaLS galaxies of the DESI imaging surveys DR9. The paper is organized as follows. In Sec. II, we present the reconstruction method and the modeling of the cross correlation. In Sec. III, we describe the data and how we process the data, which include the galaxy samples for lensing reconstruction, the imaging systematics mitigation, the galaxy samples with shear measurement and the cross correlation measurement. Sec. IV contains details of the cross-correlation analyses including the fitting to the model and the internal tests of the analysis. Summary and discussions are given in Sec. V.

II. METHOD

A. Lensing convergence map reconstruction

We aim to conduct lensing reconstruction for DECaLS galaxies based on the ideas proposed in [38, 39, 44]. In addition to galaxy flux, we leverage the information provided by

*Electronic address: qinjian@sjtu.edu.cn

†Electronic address: zhangpj@sjtu.edu.cn

‡Electronic address: yuyu22@sjtu.edu.cn

the galaxy photometry bands. Specifically, we utilize the data obtained from the g , r , and z bands and sort the galaxies into N_F flux bins for each band. In the weak lensing regime, the galaxy number overdensity of each flux bin has

$$\delta_i^L = b_i \delta_m + g_i \kappa + \delta_i^S. \quad (1)$$

Here δ_m is the underlying dark matter overdensity. b_i and g_i are the deterministic bias and the magnification coefficient in the i -th flux bin. δ_i^S denotes the term from galaxy stochasticity. Cosmic magnification modulates the galaxy density field by $g\kappa$, where κ is the lensing convergence. The magnification coefficient g is the response of δ_i^L to weak lensing, dependent on the galaxy selection criteria and observational conditions [49, 50]. For a sufficiently narrow flux bin, g is determined by the logarithmic slope of the galaxy luminosity function,

$$g = 2(a - 1), \quad a = -\frac{d \ln n(F)}{d \ln F} - 1. \quad (2)$$

For a source at redshift z_s , κ directly probes the underlying matter overdensity δ_m by

$$\kappa(\boldsymbol{\theta}, z_s) = \frac{3H_0^2 \Omega_m}{2c^2} \int_0^{\chi_s} \frac{D(\chi_s - \chi) D(\chi)}{D(\chi_s)} \delta_m(z, \boldsymbol{\theta}) (1+z) d\chi. \quad (3)$$

Where χ and χ_s are the radial comoving distances to the lens at redshift z and the source at redshift z_s , respectively. $D(\chi)$ denotes the comoving angular diameter distance, which equals χ for a flat universe.

A linear estimator of the convergence κ has the form

$$\hat{\kappa} = \sum_i w_i \delta_i^L, \quad (4)$$

The weight w_i is determined by minimizing the shot noise,

$$\left\langle \left| \sum_{i,j} w_i w_j \delta_{ij}^{\text{shot}} \right|^2 \right\rangle = \sum_{i,j} w_i w_j \frac{\bar{n}_{ij}}{\bar{n}_i \bar{n}_j}. \quad (5)$$

under conditions,

$$\sum_i w_i g_i = 1, \quad (6)$$

$$\sum_i w_i = 0. \quad (7)$$

Here, \bar{n}_i is the average galaxy surface number density of the i -th flux bin, while \bar{n}_{ij} is that both in the i -th and j -th flux bin. $\bar{n}_{ij} = 0$ if i -th and the j -th flux bin are from the same photometry band. Using the Lagrangian multiplier method, the solution is

$$w_i = \frac{1}{2} \left(\lambda_1 \sum_{j=1}^{N_F} [\mathbf{N}^{-1}]_{ij} g_j + \lambda_2 \sum_{j=1}^{N_F} [\mathbf{N}^{-1}]_{ij} \right), \quad (8)$$

where \mathbf{N} is the matrix of $\frac{\bar{n}_{ij}}{\bar{n}_i \bar{n}_j}$ and the two Lagrangian multipliers are given by

$$\lambda_1 = \frac{2 \sum_{i,j=1}^{N_F} [\mathbf{N}^{-1}]_{ij}}{(\sum_{i,j=1}^{N_F} [\mathbf{N}^{-1}]_{ij} g_i g_j) \cdot (\sum_{i,j=1}^{N_F} [\mathbf{N}^{-1}]_{ij}) - (\sum_{i,j=1}^{N_F} [\mathbf{N}^{-1}]_{ij} g_i)^2}, \quad (9a)$$

$$\lambda_2 = \frac{-2 \sum_{i,j=1}^{N_F} [\mathbf{N}^{-1}]_{ij} g_j}{(\sum_{i,j=1}^{N_F} [\mathbf{N}^{-1}]_{ij} g_i g_j) \cdot (\sum_{i,j=1}^{N_F} [\mathbf{N}^{-1}]_{ij}) - (\sum_{i,j=1}^{N_F} [\mathbf{N}^{-1}]_{ij} g_i)^2}. \quad (9b)$$

Plugging the above weight into Eq.(4), we obtain the reconstructed/estimated lensing convergence $\hat{\kappa}$.

B. Further mitigation through the convergence-shear cross-correlation

The reconstructed map can then be expressed as

$$\hat{\kappa} = A\kappa + \epsilon \delta_m + \dots. \quad (10)$$

There are two important issues to address. One is the residual galaxy clustering in the reconstructed $\hat{\kappa}$. The deterministic bias b_i , after weighting, becomes

$$\epsilon = \sum_i w_i b_i. \quad (11)$$

The other is a potential multiplicative error in the overall amplitude of $\hat{\kappa}$, which can arise from measurement error/bias in $g = 2(a - 1)$. We quantify it with a dimensionless parameter A . The neglected terms in Eq. 10 include stochastic galaxy bias, shot noise, etc. An ideal estimator would achieve $A = 1$ and $\epsilon = 0$. But our estimator only guarantees $\sum_i w_i = 0$ (Eq. 7), so we have to explicitly check whether $\epsilon \neq 0$.¹ Also, given uncertainties in the estimation of $g = 2(a - 1)$ [49, 50], we must evaluate A by the data and check whether $A = 1$.

Motivated by [36], we propose to cross-correlate our $\hat{\kappa}$ map with cosmic shear catalogs in the same patch of sky, but of multiple redshift bins. In the cross-correlation, the neglected in Eq. 10, such as stochastic galaxy bias, do not contaminate. We then have the convergence-tangential shear correlation prediction,

$$\xi_{j,\text{th}}^{\kappa\gamma}(\theta) = A \xi_j^{\kappa\gamma}(\theta) + \epsilon \xi_j^{m\gamma}(\theta). \quad (12)$$

The above correlation is the convergence/matter-tangential shear correlation. θ is the angular separation and j denotes the j -th source redshift bin of cosmic shear catalog. Since A and ϵ do not vary with j , we can simultaneously constrain cosmological parameters together with A and ϵ , through measurements

¹ This issue can be solved by the principal component analysis of the galaxy cross-correlation matrix in hyperspace of galaxy properties [48, 51]. However this method requires robust clustering measurements, inapplicable to the DR9 galaxies that we use.

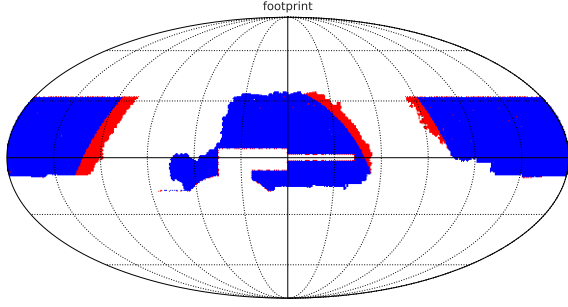


FIG. 1: The footprints of the DECaLS galaxies of LS DR9 used for weak lensing reconstruction (blue) and the DECaLS galaxies of LS DR8 with shear measurement (red). The two catalogs have a footprint overlap of 8365 deg².

of $\hat{\xi}_j^{K\gamma}$ at various source redshift bins. For the current work with the primary goal to test the feasibility of our reconstruction method, we fix the cosmology as the bestfit Planck 2018 flat Λ CDM cosmology [52] with key cosmological parameters $\Omega_m = 0.315$, $\Omega_\Lambda = 1 - \Omega_m$, $n_s = 0.965$, $h = 0.674$ and $\sigma_8 = 0.811$.

We calculate the theoretical $\xi^{K\gamma}$ and $\xi^{m\gamma}$ under the Limber approximation [53]. The correlation functions are related to the corresponding power spectra via

$$\xi^{\kappa(m)\gamma}(\theta) = \int_0^\infty \frac{d\ell\ell}{2\pi} C_\ell^{\kappa(m)\gamma} J_2(\ell\theta). \quad (13)$$

Here J_2 is the 2nd order Bessel function. $C_\ell^{K\gamma}$ and $C_\ell^{m\gamma}$ are the shear-convergence and shear-matter cross power spectrum. In a flat Universe, they are expressed by

$$C_\ell^{\kappa(m)\gamma} = \int d\chi W^{\kappa(m)} W^\gamma(\chi) \frac{1}{\chi^2} P_m \left(k = \frac{\ell}{\chi}; z \right). \quad (14)$$

Here χ is the comoving radial distance and P_m is the 3-dimensional matter power spectrum. W^κ, W^γ and W^m are the projection kernels,

$$W^{\kappa(\gamma)}(\chi) = \frac{3H_0^2\Omega_m}{2a(\chi)c^2} \int d\chi n_{\text{len}}(\chi) \frac{\chi - \chi'}{\chi}. \quad (15)$$

$$W^m(z) = n_m(z) = \frac{c}{H(z)} W^m(\chi), \quad (16)$$

where n_{len} and n_m is the normalized redshift distribution of the lens and dark matter tracers.

Then by fitting against $\hat{\xi}_{j,\text{th}}^{K\gamma}$ at multiple shear redshifts, we constrain both A and ϵ . The two then quantify the convergence map quality from both the viewpoint of detection significance (A/σ_A), and systematic errors (ϵ).

III. DATA ANALYSIS

We apply our method of lensing reconstruction to the DECaLS galaxies of the DESI imaging surveys [54] Data Release

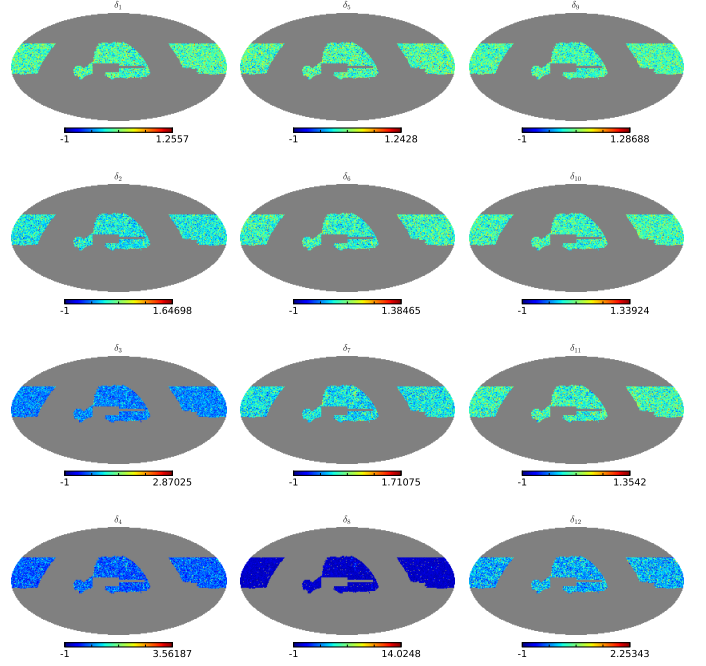


FIG. 2: The maps showing the galaxy number overdensity defined by Eq.(18), for the 12 flux bins. The HEALPix resolution parameter $N_{\text{side}} = 256$. The columns from left to right represent the g , r , and z bands, respectively. The rows increase in flux from top to bottom.

9 (LS DR9).

A. Data

The DECaLS data are processed by Tractor [55, 56]. The galaxy samples used for lensing reconstruction are created in accordance with the selection criteria outlined in section 2.1 of [57]. We summarize the main steps here. First, we select out extended imaging objects according to the morphological types provided by the TRACTOR software [58]. We choose objects that have been observed at least once in each optical band to ensure a reliable photo- z estimation. We also remove the objects within $|b| < 25.0^\circ$ (where b is the Galactic latitude) to avoid high stellar density regions. Finally, we remove any objects whose fluxes are affected by the bright stars, large galaxies, or globular clusters (maskbits 1,5,6,7,8,9,11,12,13²). The sky coverage of our selected DECaLS sample is shown in Fig.1. We apply identical selections to the publicly available random catalogues³.

For the convergence-shear cross-correlation analysis, we utilize the shear measurements from DECaLS galaxies of DESI imaging surveys DR8 (LS DR8), with a sky coverage of 8960 deg². The footprint of the DECaLS galaxies of LS

² <https://www.legacysurvey.org/dr9/bitmasks/>

³ <https://www.legacysurvey.org/dr9/files/#random-catalogues-randoms>

Sample	Magnitude Range	Galaxy Number	$\bar{n}(\text{arcmin}^{-2})$	a	g	w	band
1	(22.8, 23.0)	5590717	0.19	0.51	-0.99	-0.09	g
2	(22.6, 22.8)	5590717	0.19	1.20	0.40	-0.00	g
3	(22.3, 22.6)	5590717	0.19	1.83	1.65	0.09	g
4	(, 22.3)	5590717	0.19	2.57	3.14	0.20	g
5	(22.0, 22.2)	7740929	0.26	0.94	-0.12	0.04	r
6	(21.7, 22.0)	7740929	0.26	1.10	0.20	0.07	r
7	(21.4, 21.7)	7740929	0.26	1.47	0.94	0.06	r
8	(, 21.4)	7740929	0.26	2.11	2.22	0.03	r
9	(21.3, 21.6)	9882012	0.33	0.64	-0.72	-0.08	z
10	(21.0, 21.3)	9882012	0.33	0.65	-0.70	-0.11	z
11	(20.5, 21.0)	9882012	0.33	1.01	0.02	-0.11	z
12	(, 20.5)	9882012	0.33	1.76	1.51	-0.09	z

TABLE I: Summary of the galaxy sub-samples used for lensing reconstruction. We use galaxies in the photo- z range $0.5 < z_\kappa < 0.8$. Throughout the paper we use z_κ to denote the (photometric) redshift of galaxies used for lensing reconstruction, and use z_γ for redshift of galaxies for cosmic shear measurements. In addition to the information presented in the table, it should be noted that there are overlaps between the sub-samples in terms of the galaxies they contain. For example, sample 1 and sample 5 share a common set of 1.7×10^6 galaxies, which we denote as $n_{15} = 5.4 \times 10^6$. Similarly $n_{16} = 1.4 \times 10^6$ and $n_{17} = 0.7 \times 10^6$. However $n_{ij} = 0$ if sample i and j are from the same photometry band (e.g. $n_{12} = n_{13} = 0$).

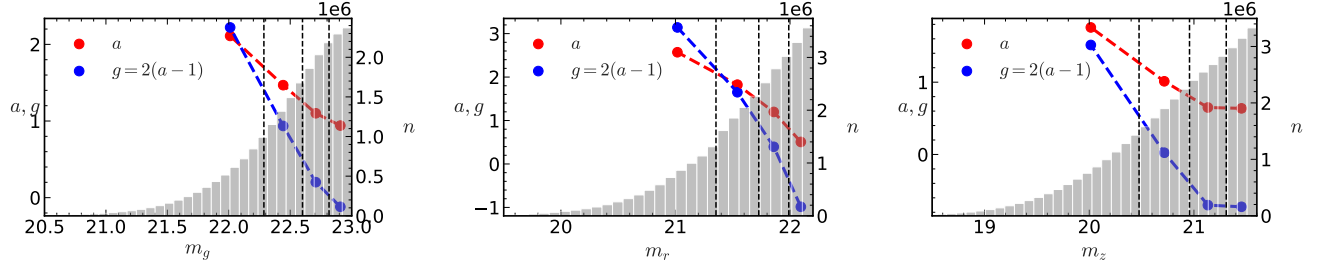


FIG. 3: The results of a and g factors for each flux bin, and histogram plot of the galaxy number counts as a function of magnitude in the three bands. The vertical black dashed lines mark the boundaries of the flux bin cuts. The left y-axis represents the values of a and g factors, while the right y-axis displays the galaxy number count.

DR8 is shown in Fig.1. These galaxies are then divided into five types according to their morphologies: PSF, SIMP, DEV, EXP, and COMP. The ellipticity $e_{1,2}$ are estimated – except for the PSF type – by a joint fit on the three optical g -, r -, and z -band. The potential measurement bias are modeled with [59–61],

$$\gamma^{\text{obs}} = (1 + m)\gamma^{\text{true}} + c.$$

The additive bias c and the multiplicative bias m is expected to come from residuals in the anisotropic PSF correction, measurement method, blending and crowding [62, 63]. This calibration is obtained by comparing with Canada–France–Hawaii Telescope (CFHT) Stripe 82 observed galaxies and Obiwan simulated galaxies [64, 65]. For both DECaLS galaxies of LS DR8 and DR9, we employ the photometric redshift based on [66], which is estimated using the g , r , and z optical bands from DECaLS and $W1$ and $W2$ infrared bands from WISE (Wide-field Infrared Survey Explorer, Wright et al. 67).

B. Reconstruction

To reconstruct the convergence map we select DECaLS galaxies of LS DR9 with $0.5 \leq z_p \leq 0.8$. Here z_p is the best-fit value of the photometric redshift of a galaxy. For each bands we select galaxies with magnitude $m_g \leq 23.0$, $m_r \leq 22.2$, $m_z \leq 21.6$. Here m_g, m_r, m_z are the magnitudes in g, r, z band. The magnitude cut of each band is set 0.1 lower than the peak position of the galaxy number counts as a function of the magnitude (Fig.3). This serves as an approximation for the flux-limit selection. Then we equally divide galaxies of each band into $N_F = 4$ flux bins. This yields 12 flux bins in total. We have other sets of choice of the magnitude cuts and N_F for consistency tests, which is described in Sec IV A. Table I shows a summary of these galaxy sub-samples.

For each flux bin, we project the 3D galaxy number density distribution to 2D sky map along the line-of-sight in the $N_{\text{side}} = 512$ resolution. We then downgrade the pixelized map to $N_{\text{side}} = 256$. We select areas pixels with an observed coverage

fraction f_β larger than a threshold $f^{\text{threshold}}$, where f_β is defined as

$$f_\beta = \frac{\sum_{i=1}^{16} \mathcal{M}_i}{\sum_i} . \quad (17)$$

Here \mathcal{M}_i is the survey mask in $N_{\text{side}} = 512$ map, which is created from the random catalogs by selecting random point with exposure time in all three bands greater than zero. This step is to minimize the impact from the footprint-induced fake clustering. For $f_\beta \geq f^{\text{threshold}}$, we assign to each pixel β its coverage fraction f_β . We use this value as a weight in the clustering measurements. We consider three choices of $f^{\text{threshold}}$ later for consistency tests but fiducial one is 0.9. After this selection, we get the galaxy overdensity for the 12 flux bins,

$$\delta_i^\beta = \frac{N_i^\beta / f^\beta}{\langle N_i^\beta / f^\beta \rangle} - 1 . \quad (18)$$

Here N_i^β is the galaxy number count of i -th flux bin in the β -th pixel. The average $\langle \dots \rangle$ is over all pixels with $f \geq f^{\text{threshold}}$. Fig.2 shows the obtained galaxy overdensity maps.

We then apply the κ estimator described in Section II to the galaxy overdensity maps. Fig.3 shows the galaxy number count as a function of magnitude and the estimated a and g factors for each magnitude bin. The numerical calculation of a of the flux bin $F \in [f_1, f_2]$ is conducted by

$$a = \frac{\log\left(\int_{f_1/(1+2\delta_F)}^{f_2/(1+2\delta_F)} n(F) dF\right) - \log\left(\int_{f_1}^{f_2} n(F) dF\right)}{2 \log(1+2\delta_F)} \quad (19)$$

We find that the numerical calculation converges for $|\delta_F| < 0.1$ and we take the result from $\delta_F = 0.02$.

The results of the $N_{ij} \equiv \frac{\bar{n}_{ij}}{\bar{n}_i \bar{n}_j}$ are shown in Fig.4. Applying Eq.(8) yields the w_i 's for each flux bin, which is shown in Fig.5. We then get the reconstructed convergence map sampled on HEALPix pixels by a weighted sum over the galaxy overdensity maps (Eq.(4)). We select pixels with $f \geq f^{\text{threshold}}$ for the cross correlation measurement.

C. Imaging systematics

Observation conditions, such as stellar contamination, Galactic extinction, sky brightness, seeing, and airmass, introduce spurious fluctuations in the observed galaxy density. Therefore, our reconstruction method based on galaxy density are potentially biased. In this work, we apply the Random Forest (RF) technique⁴ [a the machine learning based regression approach, 68] to mitigate the imaging systematics, following the procedure described in [69]. Applying the RF, a weight

factor $w_{\text{pix},i}$ for each valid pixel i will be returned. The imaging systematics will be reduced by weighting the reconstructed convergence map κ_{GRID} according to their pixel weights.

Fig.6 shows the distribution of the reconstructed convergence field, before and after the mitigation, as a function of 19 input imaging properties. If the convergence field is independent of imaging properties, one would expect the mean value of $\hat{\kappa}$ in bins of imaging properties amounts to the global mean. We can see that the reconstructed field suffers some imaging contamination at percent level. After the mitigation, the corrected density is almost flat for all imaging properties. Mitigating the imaging systematics enhances the detection significance of the weak lensing signal, which will be presented in Section IV. After mitigating the imaging systematics, we get the final convergence map κ_{GRID} . Fig.7 shows the reconstructed convergence map before and after the imaging systematics mitigation. The Weiner filtered convergence map is also presented in Fig.7. The details of the Weiner filtering procedure are presented in the Appendix.

D. Cross correlation measurement

To access the quality of the reconstructed map, we measure its cross-correlation with the DECaLS cosmic shear catalogs of LS DR8. The two catalogs have an overlap in their footprints (Fig. 1) of approximately 8365 deg². We select the shear galaxies with $0.3 < z_p < 1.0$, which yields ~ 35 million galaxy shear samples. The shear galaxies are then divided into nine photo- z bins with edges at 0.3, 0.35, 0.4, 0.45, 0.5, 0.6, 0.7, 0.8, 0.9 and 1.0. For each photo- z bin, we estimate the convergence-shear cross-correlation function by

$$\hat{\xi}^{k\gamma}(\theta) = \langle \kappa_{\text{GRID}} \gamma_t \rangle_\theta / (1 + \bar{m}) . \quad (20)$$

Here the average $\langle \dots \rangle_\theta$ is over all pixel-galaxy pairs within angular separation θ , and \bar{m} is the average shear multiplicative bias. The calculations are done using the public available code TreeCorr⁵. We use $N = 100$ Jackknife patches to estimate the covariance matrix

$$\text{Cov}_{\alpha\beta} = \frac{N-1}{N} \sum_{n=1}^{N=100} [(\hat{\xi}_n^{k\gamma}(\theta_\alpha) - \bar{\xi}^{k\gamma}(\theta_\alpha)) \times (\hat{\xi}_n^{k\gamma}(\theta_\beta) - \bar{\xi}^{k\gamma}(\theta_\beta))] . \quad (21)$$

Here $\bar{\xi}^{k\gamma}$ is the average over the 100 patches. For each photo- z bin, the data vector size is 6, and we rescale the covariance matrix following [70, 71] to get an unbiased estimation.

For the theoretical calculation of $\xi^{k\gamma}(\theta)$ and $\xi^{m\gamma}(\theta)$, we apply the Core Cosmology Library (CCL, Chisari et al. 72) and use HaloFit [73–75] to calculate the nonlinear matter power spectrum. The galaxy redshift distribution $n(z)$ are calculated for each tomographic bin, combining the photo- z distribution and a Gaussian photo- z error PDF with $\sigma_z = 0.05$ ⁶. Fig.8

⁴ <https://github.com/echaussidon/regressis>

⁵ <https://github.com/rmjarvis/TreeCorr>

⁶ We conducted tests using different assumed values of σ_z and found that they do not significantly affect the analysis results.

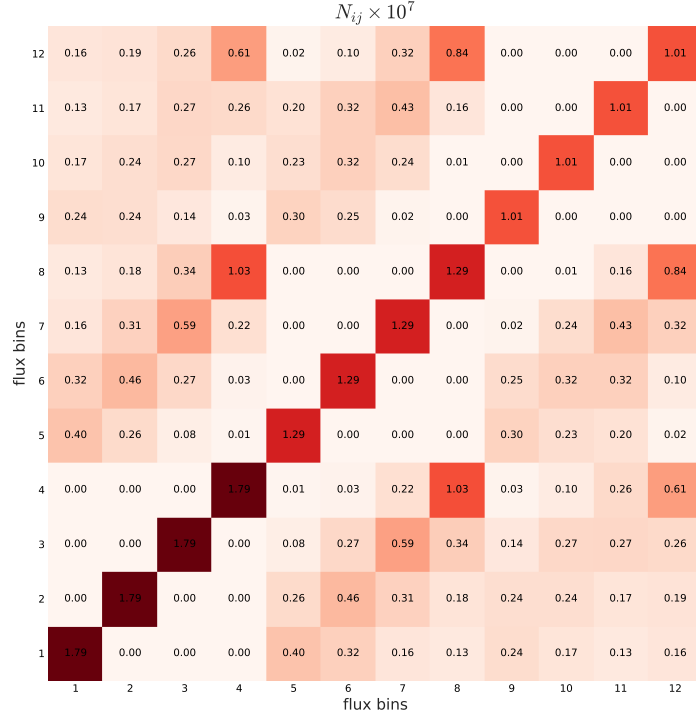


FIG. 4: The normalized galaxy surface number density matrix $N_{ij} \equiv \frac{\bar{n}_{ij}}{\bar{n}_i \bar{n}_j}$. The diagonal elements $N_{ii} \equiv \frac{1}{\bar{n}_i}$ are the normalized galaxy surface number density of each flux bin. The off-diagonal elements N_{ij} are that between the i -th and j -th flux bin.

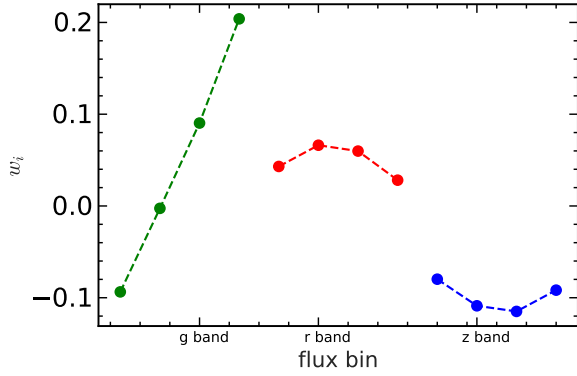


FIG. 5: The results of the weights calculated by Eq.(8) for each flux bin. The estimator for the lensing convergence is obtained by calculating the weighted average of the galaxy number overdensity.

IV. RESULTS

The results of the cross correlation are show in Fig.9. Significant cross-correlation signals are obtained. We fit the measured cross correlation against the theoretical model (Eq.(12)) and constrain the two free parameters. The constraints on A can reveal the potential biases in the lensing reconstruction or in the cross correlation analysis, if its deviation from one is observed. The constraints on ϵ indicate the level of systematic errors. The χ^2 for the fitting can be approximated by

$$\chi^2 \approx \sum_{j\alpha\beta} [\hat{\xi}_j^{K\gamma}(\theta_\alpha) - \xi_{j,\text{th}}(\theta_\alpha)] \mathbf{Cov}_j^{-1}{}_{\alpha\beta} [\hat{\xi}_j^{K\gamma}(\theta_\beta) - \xi_{j,\text{th}}(\theta_\beta)] \quad (22)$$

Here $\hat{\xi}_j^{K\gamma}$ and $\xi_{j,\text{th}}$ denote the measurement and the model in the j -th photo- z bin of shear, respectively. \mathbf{Cov} is the data covariance matrix.⁷ A and ϵ are identical for each photo- z bin and so the sum is over all the data points and photo- z bins.

The best fit is

$$(A^{\text{bestfit}} \epsilon^{\text{bestfit}})^{\mathbf{T}} = \mathbf{F}^{-1} \left[\sum_j \hat{\xi}_j^{\mathbf{T}} \mathbf{Cov}_j^{-1} \hat{\xi}_j \right], \quad (23)$$

displays the photo- z distribution of the DR9 galaxies used for lensing construction and the DR8 shear catalog. The theoretical results of $\xi^{K\gamma}(\theta)$ and $\xi^{m\gamma}(\theta)$ are shown in Fig.10. The difference in their shape and redshift dependence allow us to distinguish between the two terms.

⁷ Here we have neglected correlations between $\xi_j^{K\gamma}$ of different shear redshifts ($j_{1,2}$) arising from the four-point correlation ($\langle \gamma_{j_1 \kappa} \gamma_{j_2 \kappa} \rangle - \langle \gamma_{j_1 \kappa} \rangle \langle \gamma_{j_2 \kappa} \rangle \sim \langle \gamma_{j_1 \kappa} \rangle \langle \gamma_{j_2 \kappa} \rangle + \langle \gamma_{j_1} \gamma_{j_2} \rangle \langle \kappa \kappa \rangle$). For the current data, it is negligible comparing to the shape measurement error in γ and shot noise in κ .

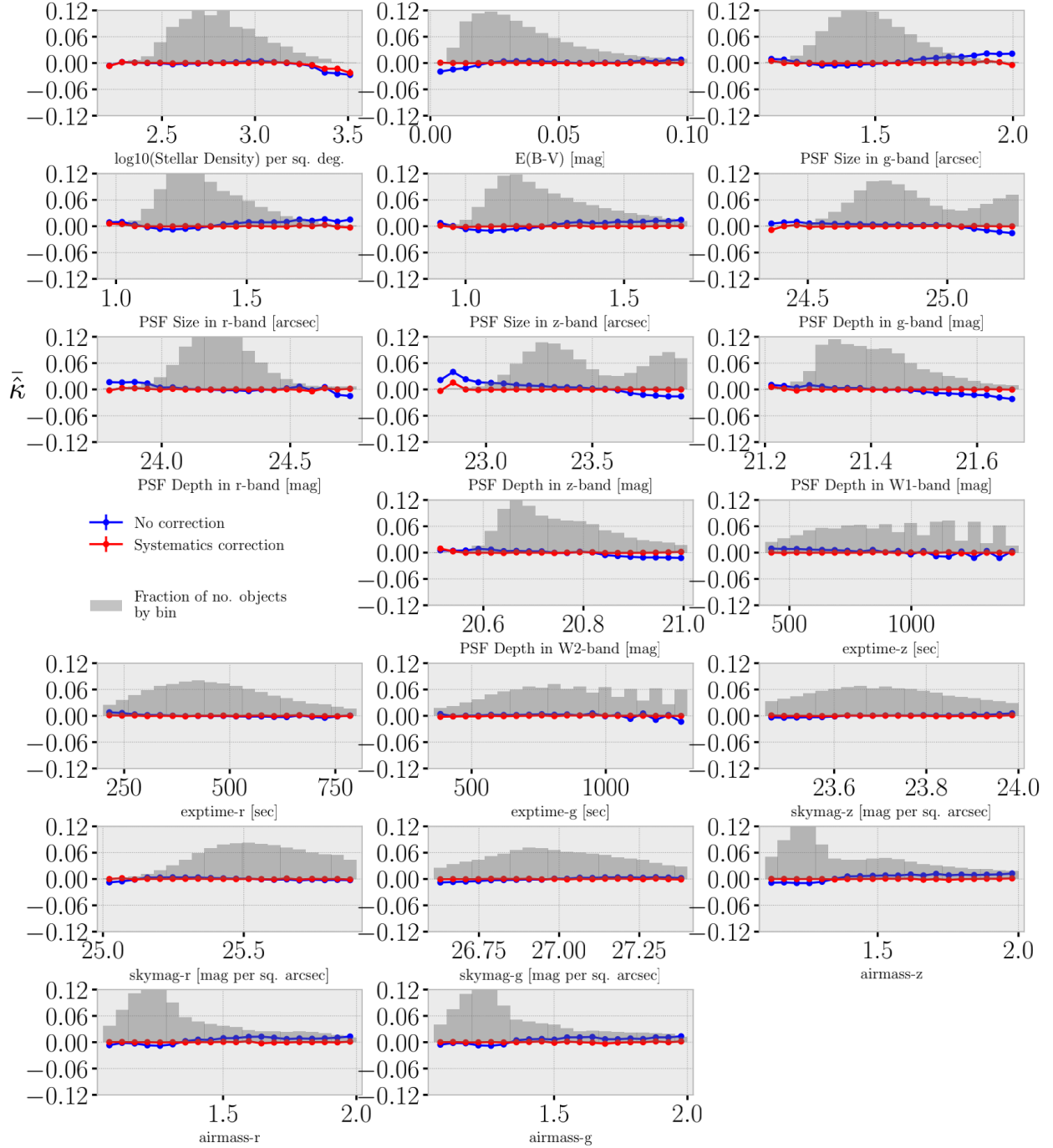


FIG. 6: Average value of the reconstructed convergence field as a function of 19 input imaging maps. The blue/red lines show the relative density before/after the systematics correction. The histogram is the fraction of pixels in bins of imaging properties, which is used to estimate the errors as the standard deviation of the convergence field in bins. After mitigating the imaging systematics, the convergence field show little fluctuation with respect to imaging properties.

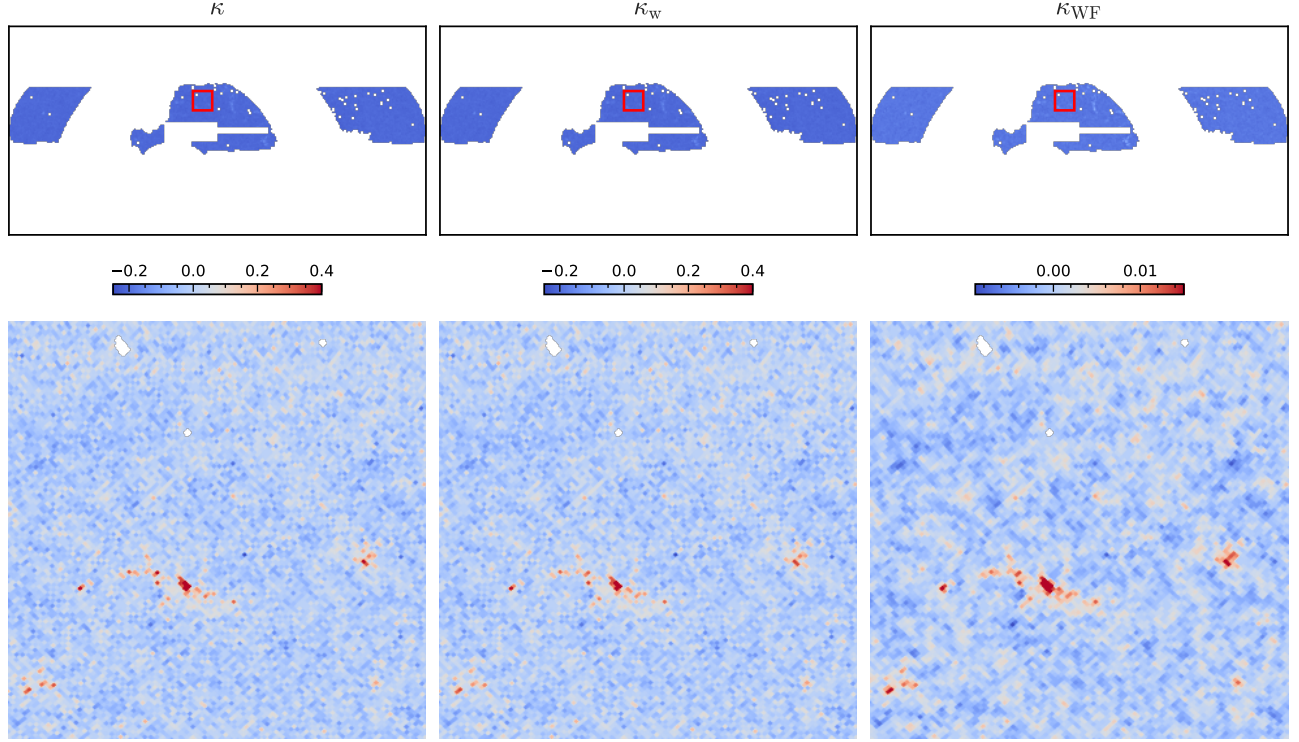


FIG. 7: The reconstructed lensing convergence map κ_{GRID} sampled on HEALPix pixels with $N_{\text{side}} = 256$. The left panel shows the map before the imaging systematics mitigation, and the middle panel shows the map after the mitigation. The right panel shows the map after the mitigation and the application of the Wiener filter. The lower panels correspond to zoomed-in views of the areas indicated by the red box in the upper panels.

where

$$\xi_j \equiv \begin{pmatrix} \xi_j^{\kappa\gamma}(\theta_1) & \xi_j^{\kappa m}(\theta_1) \\ \xi_j^{\kappa\gamma}(\theta_2) & \xi_j^{\kappa m}(\theta_2) \\ \vdots & \vdots \\ \xi_j^{\kappa\gamma}(\theta_n) & \xi_j^{\kappa m}(\theta_n) \end{pmatrix}; \hat{\xi}_i \equiv \begin{pmatrix} \hat{\xi}_i^{\kappa\gamma}(\theta_1) \\ \hat{\xi}_i^{\kappa\gamma}(\theta_2) \\ \vdots \\ \hat{\xi}_i^{\kappa\gamma}(\theta_n) \end{pmatrix}. \quad (24)$$

The associated errors and covariance matrix of the constraints are given by \mathbf{F}^{-1} . \mathbf{F} is the fisher matrix of A and ϵ ,

$$\mathbf{F} = \begin{pmatrix} \sum_{j\alpha\beta} \xi_{j,\alpha}^{\kappa\gamma} \mathbf{Cov}_{j,\alpha\beta}^{-1} \xi_{j,\beta}^{\kappa\gamma} & \sum_{j\alpha\beta} \xi_{j,\alpha}^{\kappa\gamma} \mathbf{Cov}_{j,\alpha\beta}^{-1} \xi_{j,\beta}^{\kappa m} \\ \sum_{j\alpha\beta} \xi_{j,\alpha}^{\kappa m} \mathbf{Cov}_{j,\alpha\beta}^{-1} \xi_{j,\beta}^{\kappa\gamma} & \sum_{j\alpha\beta} \xi_{j,\alpha}^{\kappa m} \mathbf{Cov}_{j,\alpha\beta}^{-1} \xi_{j,\beta}^{\kappa m} \end{pmatrix}$$

Fig.11 shows the results of the constraints. According to A , we detect a convergence-shear cross-correlation signal with $S/N \equiv A/\sigma_A \approx 10$. According to ϵ , the galaxy intrinsic clustering is suppressed by a factor by a factor ~ 50 , to a level of -0.02 ± 0.02 . The residual galaxy clustering contamination in the $\hat{\kappa}$ map is consistent with zero. The best-fit to the cross-correlation is shown in Fig.9, and the two components $A\xi^{\kappa\gamma}$

and $\epsilon\xi^{m\gamma}$ are also highlighted in the figure. The $\epsilon\xi^{m\gamma}$ term is subdominant for all cases.

Unfortunately, a significant deviation from one is detected in A . There are possible uncertainties that may lead to this bias, such as the S_8 tension between the low- z and the CMB measurements, the photo- z error, and the shear measurement error. Out of all the factors, the measurement error/bias in $g = 2(a - 1)$ should be the primary cause of the discrepancy of factor ~ 2 . In this work it is determined by flux-based method, i.e. the logarithmic slope of the luminosity function (Eq.(2)). It is unbiased if the galaxy samples are strictly flux-limited. However the real galaxy samples are a complex selection of flux, color, position and shape. Consequently, biases arise in flux-based methods when estimating the magnification coefficient in real samples. Even when taking into account a simplified survey selection function, this bias may reach $\sim 2 - 3$ [49, 50], comparable to the bias observed in this work. The actual magnification coefficients could be investigated by forward modeling the real selection functions [e.g., 50], which will help reduce the bias. We leave it for future studies.

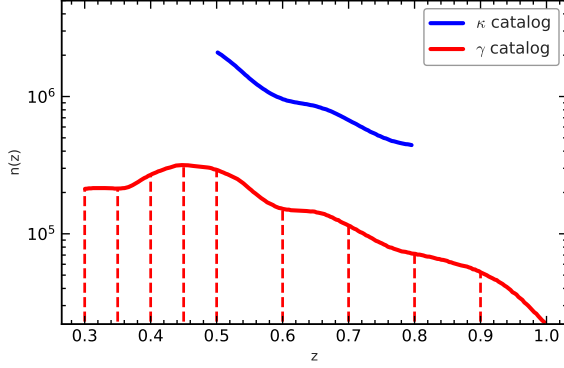


FIG. 8: The photometric redshift distributions of the DR9 galaxies used for lensing construction (blue line) and the DR8 galaxies with shear measurement (red line). The vertical dashed lines represent the boundaries of the photo- z bins for the shear catalog, defined for cross correlation analysis.

Table III lists the results of χ_{\min}^2 and χ_{null}^2 to demonstrate the goodness of fit to the model, where the χ_{null}^2 and χ_{\min}^2 is defined by

$$\chi_{\text{null}}^2 = \sum_{j\alpha\beta} [\hat{\xi}_j^{K\gamma}(\theta_\alpha)] \mathbf{Cov}_j^{-1}{}_{\alpha\beta} \times [\hat{\xi}_j^{K\gamma}(\theta_\beta)], \quad (25)$$

$$\chi_{\min}^2 = \sum_{j\alpha\beta} [\hat{\xi}_j^{K\gamma}(\theta_\alpha) - \xi_{j,\text{th}}^{\text{bestfit}}(\theta_\alpha)] \mathbf{Cov}_j^{-1}{}_{\alpha\beta} \times [\hat{\xi}_j^{K\gamma}(\theta_\beta) - \xi_{j,\text{th}}^{\text{bestfit}}(\theta_\beta)], \quad (26)$$

where

$$\xi_{\text{th}}^{\text{bestfit}} = A^{\text{bestfit}} \xi^{\kappa\gamma} + \epsilon^{\text{bestfit}} \xi^{m\gamma}. \quad (27)$$

The degree-of-freedom (d.o.f) of the fitting is 52 and the $\chi_{\min}^2 \simeq 59$. Therefore, the two parameter fitting returns reasonable $\chi_{\min}^2/\text{d.o.f.} \sim 1$. This means that shape of the measured cross-correlation agrees with the model prediction, and provides support that the detected signal is cosmological in origin. With 54 non-independent data points and the full covariance, $\chi_{\text{null}}^2 = 367.6$ and $\chi_{\min}^2 = 58.7$ with respect to the null and to the model, respectively. According to the data-driven signal-to-noise ratio $\sqrt{\chi_{\text{null}}^2}$, we get 19.1σ detection of a non-zero cross-correlation signal. According to the fitting-driven signal-to-noise ratio $\sqrt{\chi_{\text{null}}^2 - \chi_{\min}^2}$, the significance is $\sim 10.7\sigma$. We compared the results before and after the imaging systematics mitigation in Table III. It shows that the fitting results are consistent, and after the mitigation, both $\sqrt{\chi_{\text{null}}^2 - \chi_{\min}^2}$ and A/σ_A exhibit an increase from 15.1 to 17.6 and 8.5 to 10.8, respectively.

A. Internal test

We test the impact of several factors in the analysis, which are summarized in Table III. First, we compare the results

	baseline	A=0	A=1	$\epsilon=0$
χ_{\min}^2	58.7	169.2	90.3	59.9
AIC	62.8	171.3	92.3	62.0

TABLE II: χ_{\min}^2 and AIC scores for the baseline and the three alternative models.

for $f^{\text{threshold}} = 0.5, 0.7, 0.9$. Larger $f^{\text{threshold}}$ indicates more stringent selection of the pixels of galaxy number overdensity map. Table III shows that the impact of $f^{\text{threshold}}$ is small, and the fitting result is stable for different $f^{\text{threshold}}$.

Second, we test the cases of $N_F = 2, 3, 4$ and find that the constraints on A and ϵ are stable for different N_F . The $\epsilon = \sum_i w_i b_i$ depends on the galaxy biases in the selected flux bins and, consequently, on the number of flux bins N_F . The ϵ is consistently to be a minimal value for different N_F . It indicates that our method of eliminating the galaxy intrinsic clustering is robust.

Third, we test the influence of the magnitude cut on the results. We select galaxies which are 0.5 magnitude brighter than the baseline set. The first case involves selecting galaxies that are 0.5 magnitudes brighter across all three bands, denoted as $m_{g,r,z} - 0.5$. The other three cases involve selecting galaxies that are 0.5 magnitudes brighter in each band individually, denoted as $m_g - 0.5$, $m_r - 0.5$ and $m_z - 0.5$. As shown in Table III, ϵ remains minimal for all the cases. However the results of A are significantly affected by the magnitude cuts. This discrepancy observed in A is reasonable. It supports our hypothesis that the error/bias in $g = 2(a - 1)$ is the primary contributor to the multiplicative error in the overall amplitude of $\hat{\kappa}$. A brighter magnitude cut of 0.5 results in a decrease of $\sim 30\text{--}40\%$ in the number of galaxies for a particular photometry band. It then results in modifications to the selection functions of the galaxy samples, thereby inducing alterations in the magnification coefficient. The level of the bias can extend up to a factor of 3 for the $m_{r,g,z} - 0.5$ case, which is unlikely to result from other systematics. The impact of magnitude cuts on the magnification coefficient is also investigated in [49]. Their results support our findings, showing that modification in the magnitude cut can lead to the magnification coefficient ranging from 1.5 to 3.0.

In addition, Table III presents the comparison of fitting results before and after mitigating the imaging systematics for all the tests investigated above. Across all cases, the fitting results are consistent and exhibit enhancements in the S/N after the mitigation, indicating the effectiveness and robustness of the mitigation procedure.

B. Model selection

Performing an Akaike information criterion (AIC) analysis can provide valuable insights into which model is the most suitable for explaining the observed data. In this part, we modify the theoretical template to facilitate the comparison of different models. In addition to the baseline model described by Eq. (12), we also consider alternative models which we

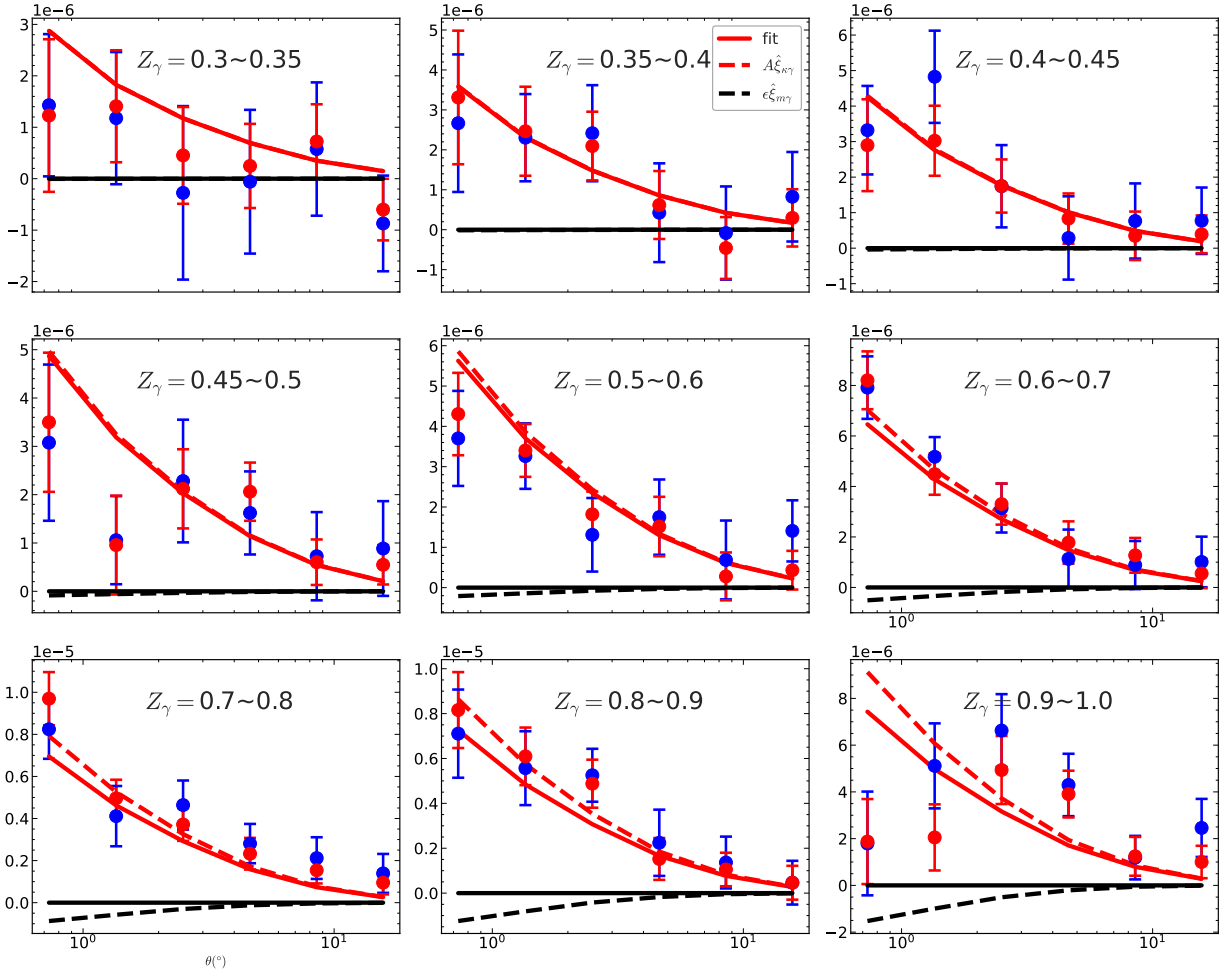


FIG. 9: Measured cross correlation function between the reconstructed convergence and the shear. The red/blue data points denotes the results with/without imaging systematics mitigation. The solid lines represent the best-fit, where the fitted values of A and ϵ are the same for each shear bin. The dashed lines denote the two components of the best-fit model. For clarity we only show the best-fit for the measurements after the mitigation. The comparison of the fitting before and after the mitigation is summarized in Table III.

keep either A or ϵ fixed. We compare four cases: the baseline model, fixing $A = 0$, fixing $A = 1$, and fixing $\epsilon = 0$. For each model we repeat the fitting process and then calculate the AIC, which can be expressed, to second-order, as:

$$\text{AIC}_c = -2 \ln p(\lambda_{\text{bestfit}} | D) + 2N_\lambda + \frac{2N_\lambda + 1}{N_D - N_\lambda - 1}.$$

Here N_λ is the number of parameters, N_D is the number of data points, p is the likelihood which is Gaussian in our case and $p(\lambda_{\text{bestfit}} | D)$ is the value for the best-fit parameters. The "best" model has the smallest AIC. If another model's AIC is larger by 10 or more, this model should be ruled out. If the difference is less than 2, the two models can not be really distinguished.

Table II shows the results of χ^2_{min} (the minimum χ^2 value obtained during fitting) and AIC. The model that fixes $\epsilon = 0$ has the lowest AIC score and is 0.8 lower than that of the baseline model. It reinforces the conclusion that the residual galaxy clustering contamination in the $\hat{\kappa}$ map is insignificant.

The model that fixes $A = 0$ has an AIC score that is roughly 108 higher than the baseline, ruling out null detection of weak lensing signal. The model that fixes $A = 1$ displays an AIC score ~ 30.0 higher than the baseline. This implies the significance of the multiplicative error in the overall amplitude of $\hat{\kappa}$, which we attribute to the limitation of the flux-based method in accurately estimating the magnification coefficient.

C. Impact of the galaxy intrinsic clustering

To eliminate the average galaxy clustering in the lensing reconstruction, we initially employed the condition $\sum w_i = 0$. However, we can reevaluate the impact of average galaxy clustering by modifying the condition to

$$\sum_i w_i \hat{b}_i = 0. \quad (28)$$

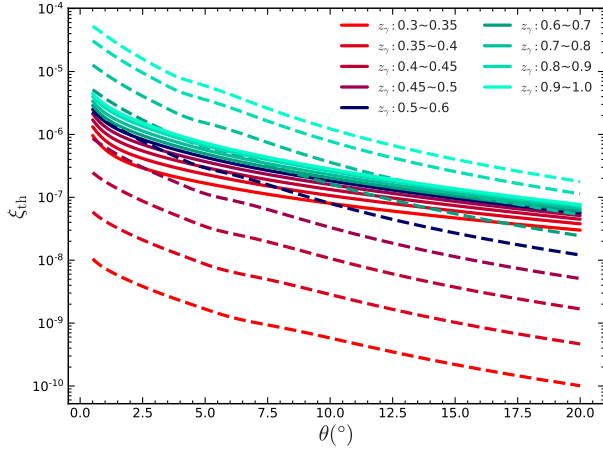


FIG. 10: The theoretical cross correlation templates, under the Planck 2018 cosmology. Different colors are used to distinguish the results of different photo- z bins of the shear. The signal term ξ^{KY} is represented by the solid lines, while the contamination term ξ^{km} is denoted by the dashed lines.

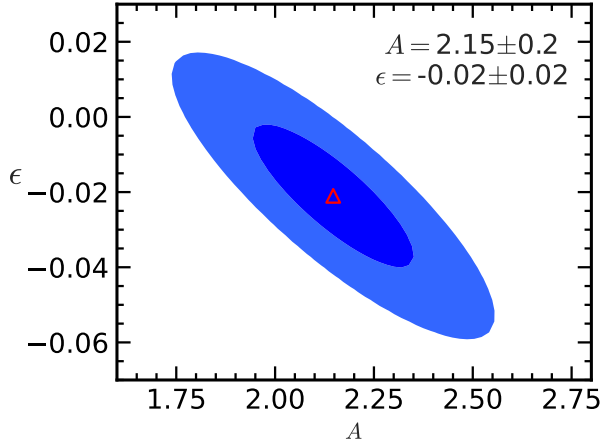


FIG. 11: Contour plot of the constraints on A and ϵ , where the triangular point denote the best-fit value. The contour levels are 1- and 2- σ .

Here, the values of \hat{b}_i are artificially selected. Setting all \hat{b}_i 's equal to a constant reduces to the original condition. Selecting forms that \hat{b}_i 's deviate from a constant will enhance the impact of the galaxy clustering. The results of ϵ are expected to be dependent on the form of \hat{b}_i 's, while those of A are not. We use a simple form of \hat{b}_i as a demonstration. For each band, we set \hat{b}_i for the four flux bins to be

$$1 - 2\Delta\hat{b}, 1 - \Delta\hat{b}, 1 + \Delta\hat{b}, 1 + 2\Delta\hat{b} \quad (29)$$

The only parameter is $\Delta\hat{b}$, which we set to be identical for each band. We sample $\Delta\hat{b}$ in the range $[-0.25, 0.25]$ with bin width 0.05. For each $\Delta\hat{b}$ we repeat the lensing reconstruction procedure and conduct the cross-correlation analysis to obtain the constraints on A and ϵ .

Fig.12 shows the impact of $\Delta\hat{b}$ on the results of constraints. The best fit of A is insensitive to the choice of $\Delta\hat{b}$, as expected, showing the stability of the reconstruction. However, the results of ϵ exhibit significant dependence on $\Delta\hat{b}$, and tend to have a linear relation with $\Delta\hat{b}$. Its deviation from zero is significant when $|\Delta\hat{b}|$ differs considerably from zero. Therefore by varying the condition to Eq. (28), we revealed the evidence of galaxy clustering which contaminates the cosmic magnification. The initial condition for the baseline (i.e. $\Delta\hat{b} = 0$ s.t. $\sum w_i = 0$) is almost optimal in terms of reducing this contamination. Because ϵ fluctuates around zero when $\Delta\hat{b}$ is near zero and the $S/N \equiv A/\sigma_A$ reaches maximum when $\Delta\hat{b} = 0$ (the right panel in Fig.12).

The above results imply that the galaxy deterministic biases exhibit minimal dependence on the magnitude, such that $\sum w_i \sim 0$. It agrees with recent findings with hydrodynamic simulations, including one based on TNG [76, 77] by [51] and another using CosmoDC2 [78] by our companion work [48]. Fig.12 also shows that the imaging mitigation enhances S/N for all the investigated cases of $\Delta\hat{b}$.

D. Impact of the shear redshifts

The parameters A and ϵ characterize the reconstructed lensing convergence and are therefore independent of the shear catalog utilized. Consequently, the constraints on A and ϵ are expected to remain consistent when different shear catalogs are employed for cross-correlation analysis. In this part, we investigate the impact of selecting different redshift bins for the shear by systematically excluding one shear redshift bin at a time. We then perform cross-correlation analysis and constrain A and ϵ using the remaining redshift bins. The results of this test are presented in Fig. 13. For all cases except the redshift bin $[0.9 - 1.0]$, the constraints on A and ϵ align with the baseline set within the 1σ error range. The discrepancy observed in the redshift $[0.9 - 1.0]$ can be attributed to the lower galaxy number density (Fig.8) and consequently, a less accurate detection of the correlation function (Fig.10).

V. SUMMARY AND DISCUSSION

Based on cosmic magnification, we reconstruct weak lensing convergence map from the DECaLS DR9 galaxy catalog. Notably, this represents the first instance of a directly measured lensing map from magnification, covering a quarter of the sky. It is done by weighing overdensity maps of galaxies in different magnitude bins and different photometry bands. To test validity of the reconstruction, we make cross correlation to the galaxy shear measurement and compare to the theoretical model. We find that the galaxy intrinsic clustering is well eliminated by our method and we get $\sim 10\sigma$ detection of the convergence-shear cross correlation.

A discrepancy in the lensing amplitude of factor ~ 2 is found. The most likely cause for this discrepancy is the inaccuracies in measuring the magnification coefficient, which is

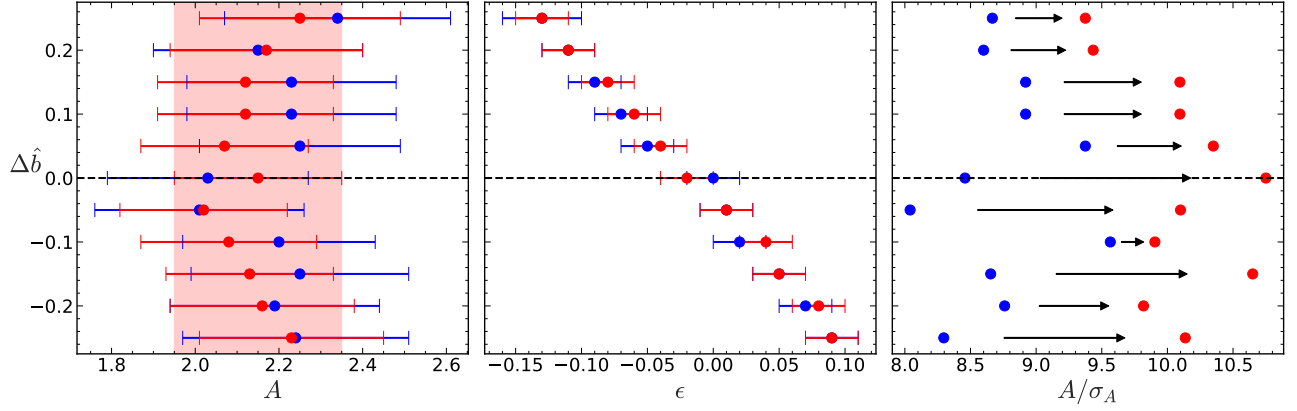


FIG. 12: Impact of varying the condition $\sum w_i \hat{b}_i$ on the constraints of A (the left panel), ϵ (the middle panel) and A/σ_A (the right panel). The red/blue data points denotes the results with/without imaging systematics mitigation. In the left panel, the shaded regions represent the 1σ error in the constraint on A for the baseline configuration, which corresponds to $\Delta \hat{b} = 0$ and includes imaging systematics mitigation.

	A	ϵ	χ^2_{\min}	χ^2_{null}	$\sqrt{\chi^2_{\text{null}} - \chi^2_{\min}}$	A/σ_A
baseline	$2.15 \pm 0.20 (2.03 \pm 0.24)$	$-0.02 \pm 0.02 (-0.00 \pm 0.02)$	58.7(59.2)	367.6(286.7)	17.6(15.1)	10.8(8.5)
$f=0.5$	$2.00 \pm 0.20 (2.16 \pm 0.23)$	$-0.00 \pm 0.02 (-0.02 \pm 0.02)$	55.0(56.9)	393.2(313.7)	18.4(16.0)	10.0(9.4)
$f=0.7$	$2.10 \pm 0.20 (2.11 \pm 0.25)$	$-0.01 \pm 0.02 (-0.02 \pm 0.02)$	53.0(61.2)	404.5(266.8)	18.8(14.3)	10.5(8.4)
$N_F = 2$	$2.14 \pm 0.21 (2.21 \pm 0.24)$	$-0.01 \pm 0.02 (-0.01 \pm 0.02)$	58.5(63.8)	389.4(322.8)	18.2(16.1)	10.2(9.2)
$N_F = 3$	$1.79 \pm 0.20 (1.85 \pm 0.23)$	$0.02 \pm 0.02 (0.01 \pm 0.02)$	55.9(61.0)	363.9(307.8)	17.6(15.7)	8.9(8.0)
$m_{g,r,z} - 0.5$	$3.09 \pm 0.30 (2.97 \pm 0.36)$	$-0.08 \pm 0.03 (-0.06 \pm 0.03)$	41.1(43.2)	242.3(208.3)	14.2(12.8)	10.3(8.2)
$m_g - 0.5$	$2.09 \pm 0.25 (2.09 \pm 0.33)$	$-0.00 \pm 0.02 (-0.00 \pm 0.03)$	47.5(41.8)	248.2(172.4)	14.2(11.4)	8.4(6.3)
$m_r - 0.5$	$1.24 \pm 0.19 (1.45 \pm 0.23)$	$0.06 \pm 0.02 (0.05 \pm 0.02)$	63.5(63.1)	348.2(277.6)	16.9(14.7)	6.5(6.3)
$m_z - 0.5$	$2.13 \pm 0.20 (2.24 \pm 0.25)$	$-0.04 \pm 0.02 (-0.05 \pm 0.02)$	48.0(48.2)	288.3(221.9)	15.5(13.2)	10.7(9.0)

TABLE III: The impact of $f^{\text{threshold}}$, N_F , the three bands magnitude cuts and the imaging systematics mitigation on the analysis. The fiducial sets are $f^{\text{threshold}} = 0.9$, $N_F = 4$, $m_g = 23.0$, $m_r = 22.2$, $m_z = 21.6$. The d.o.f. = 52. The main table shows the results after the mitigation, while in parentheses are the results before the mitigation.

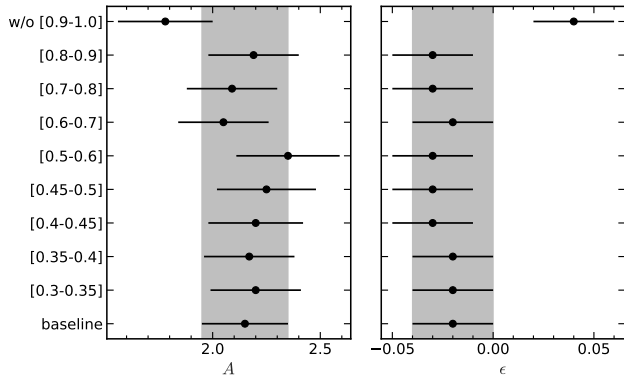


FIG. 13: Impact of the shear redshifts on the constraints of A (the left panel) and ϵ (the right panel). We drop one shear redshift bin at a time, and perform the cross correlation analysis and constrain the parameters with the remaining bins. The y-axis denote the shear redshift bin that is dropped. The shadow regions shows the 1σ error of the constraints for the baseline set (i.e., all the bins are included).

estimated using the logarithmic slope of the luminosity function. However, to confirm this speculation, we need to perform forward modeling of the DR9 galaxy selection function and correct the estimation of the magnification coefficient. This is our next step in the research project. Our primary focus is on the cross-correlation analysis since the auto-correlation of the reconstructed convergence map is significantly affected by the weighted shot noise [48]. Existing data such as DES [8] and HSC [10] have greater survey depth and higher galaxy number than DECaLS. We plan to analyze these data to improve the magnification based lensing reconstruction. It will enable us to thoroughly account for the model's cosmology dependence, more realistic modeling of the photo- z distribution, the intrinsic alignment of galaxies, and potential contamination from the extragalactic dust.

Acknowledgements

The authors thank Jun Zhang for useful discussions. This work is supported by National Science Foundation of China (11621303, 12273020, 11890690), the National Key R&D

Program of China (2020YFC2201602), the China Manned Space Project (#CMS-CSST-2021-A02 & CMS-CSST-2021-A03), and the Fundamental Research Funds for the Central Universities.

-
- [1] M. Bartelmann and P. Schneider, *Phys. Rep.* **340**, 291 (2001), astro-ph/9912508.
- [2] M. Kilbinger, *Reports on Progress in Physics* **78**, 086901 (2015), 1411.0115.
- [3] M. Bartelmann and P. Schneider, *Phys. Rep.* **340**, 291 (2001), astro-ph/9912508.
- [4] H. Hoekstra and B. Jain, *Annual Review of Nuclear and Particle Science* **58**, 99 (2008), 0805.0139.
- [5] L. Van Waerbeke, H. Hildebrandt, J. Ford, and M. Milkeraitis, *ApJ* **723**, L13 (2010), 1004.3793.
- [6] L.-P. Fu and Z.-H. Fan, *Research in Astronomy and Astrophysics* **14**, 1061-1120 (2014).
- [7] M. Kilbinger, *Reports on Progress in Physics* **78**, 086901 (2015), 1411.0115.
- [8] Dark Energy Survey Collaboration, T. Abbott, F. B. Abdalla, J. Aleksić, S. Allam, A. Amara, D. Bacon, E. Balbinot, M. Banerji, K. Bechtol, et al., *MNRAS* **460**, 1270 (2016), 1601.00329.
- [9] J. T. A. de Jong, G. A. Verdoes Kleijn, K. H. Kuijken, and E. A. Valentijn, *Experimental Astronomy* **35**, 25 (2013), 1206.1254.
- [10] H. Aihara, N. Arimoto, R. Armstrong, S. Arnouts, N. A. Bahcall, S. Bickerton, J. Bosch, K. Bundy, P. L. Capak, J. H. H. Chan, et al., *PASJ* **70**, S4 (2018), 1704.05858.
- [11] T. Hamana, M. Shirasaki, S. Miyazaki, C. Hikage, M. Oguri, S. More, R. Armstrong, A. Leauthaud, R. Mandelbaum, H. Miyatake, et al., *PASJ* **72**, 16 (2020), 1906.06041.
- [12] M. Asgari, C.-A. Lin, B. Joachimi, B. Giblin, C. Heymans, H. Hildebrandt, A. Kannawadi, B. Stözlner, T. Tröster, J. L. van den Busch, et al., *A&A* **645**, A104 (2021), 2007.15633.
- [13] B. Giblin, C. Heymans, M. Asgari, H. Hildebrandt, H. Hoekstra, B. Joachimi, A. Kannawadi, K. Kuijken, C.-A. Lin, L. Miller, et al., *A&A* **645**, A105 (2021), 2007.01845.
- [14] A. Loureiro, L. Whittaker, A. Spurio Mancini, B. Joachimi, A. Cuceu, M. Asgari, B. Stözlner, T. Tröster, A. H. Wright, M. Bilicki, et al., *A&A* **665**, A56 (2022), 2110.06947.
- [15] A. Amon, D. Gruen, M. A. Troxel, N. MacCrann, S. Dodelson, A. Choi, C. Doux, L. F. Secco, S. Samuroff, E. Krause, et al. (DES Collaboration), *Phys. Rev. D* **105**, 023514 (2022), URL <https://link.aps.org/doi/10.1103/PhysRevD.105.023514>.
- [16] L. F. Secco, S. Samuroff, E. Krause, B. Jain, J. Blazek, M. Raveri, A. Campos, A. Amon, A. Chen, C. Doux, et al. (DES Collaboration), *Phys. Rev. D* **105**, 023515 (2022), URL <https://link.aps.org/doi/10.1103/PhysRevD.105.023515>.
- [17] X. Li, T. Zhang, S. Sugiyama, R. Dalal, M. M. Rau, R. Mandelbaum, M. Takada, S. More, M. A. Strauss, H. Miyatake, et al., *arXiv e-prints arXiv:2304.00702* (2023), 2304.00702.
- [18] R. D. Blandford and R. Narayan, *ARA&A* **30**, 311 (1992).
- [19] M. Bartelmann and R. Narayan, in *Dark Matter*, edited by S. S. Holt and C. L. Bennett (1995), vol. 336 of *American Institute of Physics Conference Series*, pp. 307–319, astro-ph/9411033.
- [20] A. H. Bauer, E. Gaztañaga, P. Martí, and R. Miquel, *Monthly Notices of the Royal Astronomical Society* **440**, 3701 (2014), <https://academic.oup.com/mnras/article-pdf/440/4/3701/3913172/stu530.pdf>, URL <https://app.dimensions.ai/details/publication/pub.1059915677>.
- [21] F. Bellagamba, M. Sereno, M. Roncarelli, M. Maturi, M. Radovich, S. Bardelli, E. Puddu, L. Moscardini, F. Getman, H. Hildebrandt, et al., *MNRAS* **484**, 1598 (2019), 1810.02827.
- [22] I. Chiu, J. P. Dietrich, J. Mohr, D. E. Applegate, B. A. Benson, L. E. Bleem, M. B. Bayliss, S. Bocquet, J. E. Carlstrom, R. Capasso, et al., *MNRAS* **457**, 3050 (2016), 1510.01745.
- [23] I. N. Chiu, K. Umetsu, R. Murata, E. Medezinski, and M. Oguri, *MNRAS* **495**, 428 (2020), 1909.02042.
- [24] R. Scranton, B. Ménard, G. T. Richards, R. C. Nichol, A. D. Myers, B. Jain, A. Gray, M. Bartelmann, R. J. Brunner, A. J. Connolly, et al., *ApJ* **633**, 589 (2005), astro-ph/0504510.
- [25] A. H. Bauer, C. Baltay, N. Ellman, J. Jerke, D. Rabinowitz, and R. Scalzo, *ApJ* **749**, 56 (2012), 1202.1371.
- [26] C. B. Morrison, R. Scranton, B. Ménard, S. J. Schmidt, J. A. Tyson, R. Ryan, A. Choi, and D. M. Wittman, *MNRAS* **426**, 2489 (2012), 1204.2830.
- [27] A. Tudorica, H. Hildebrandt, M. Tewes, H. Hoekstra, C. B. Morrison, A. Muzzin, G. Wilson, H. K. C. Yee, C. Lidman, A. Hicks, et al., *A&A* **608**, A141 (2017), 1710.06431.
- [28] L. Bonavera, M. M. Cueli, J. González-Nuevo, T. Ronconi, M. Migliaccio, A. Lapi, J. M. Casas, and D. Crespo, *A&A* **656**, A99 (2021), 2109.12413.
- [29] D. Crespo, J. González-Nuevo, L. Bonavera, M. M. Cueli, J. M. Casas, and E. Goitia, *A&A* **667**, A146 (2022), 2210.17318.
- [30] B. Ménard, R. Scranton, M. Fukugita, and G. Richards, *MNRAS* **405**, 1025 (2010), 0902.4240.
- [31] B. Jain and M. Lima, *MNRAS* **411**, 2113 (2011), 1003.6127.
- [32] F. Schmidt, A. Leauthaud, R. Massey, J. Rhodes, M. R. George, A. M. Koekemoer, A. Finoguenov, and M. Tanaka, *The Astrophysical Journal* **744**, L22 (2012), URL <http://dx.doi.org/10.1088/2041-8205/744/2/L22>.
- [33] E. M. Huff and G. J. Graves, *ApJ* **780**, L16 (2014).
- [34] C. A. J. Duncan, C. Heymans, A. F. Heavens, and B. Joachimi, *Monthly Notices of the Royal Astronomical Society* **457**, 764–785 (2016), URL <http://dx.doi.org/10.1093/mnras/stw027>.
- [35] M. Garcia-Fernandez, E. Sanchez, I. Sevilla-Noarbe, E. Suchyta, E. M. Huff, E. Gaztanaga, Aleksić, J. , R. Ponce, F. J. Castander, et al., *MNRAS* **476**, 1071 (2018).
- [36] X. Liu, D. Liu, Z. Gao, C. Wei, G. Li, L. Fu, T. Futamase, and Z. Fan, *Phys. Rev. D* **103**, 123504 (2021), 2104.13595.
- [37] J. Yao, H. Shan, P. Zhang, E. Jullo, J.-P. Kneib, Y. Yu, Y. Zu, D. Brooks, A. de la Macorra, P. Doel, et al., *MNRAS* **524**, 6071 (2023), 2301.13434.
- [38] P. Zhang and U.-L. Pen, *Phys. Rev. Lett.* **95**, 241302 (2005), astro-ph/0506740.
- [39] X. Yang and P. Zhang, *MNRAS* **415**, 3485 (2011), 1105.2385.
- [40] P. Zhang, J. Zhang, and L. Zhang, *MNRAS* **484**, 1616 (2019).
- [41] X. Yang, P. Zhang, J. Zhang, and Y. Yu, *MNRAS* **447**, 345 (2015).

- [42] X. Yang, J. Zhang, Y. Yu, and P. Zhang, *ApJ* **845**, 174 (2017), 1703.01575.
- [43] P. Zhang, X. Yang, J. Zhang, and Y. Yu, *ApJ* **864**, 10 (2018), 1807.00443.
- [44] S.-T. Hou, Y. Yu, and P.-J. Zhang, *Research in Astronomy and Astrophysics* **21**, 247 (2021), 2106.09970.
- [45] S. Bonoli and U. L. Pen, *MNRAS* **396**, 1610 (2009), 0810.0273.
- [46] N. Hamaus, U. Seljak, V. Desjacques, R. E. Smith, and T. Baldauf, *Phys. Rev. D* **82**, 043515 (2010), 1004.5377.
- [47] T. Baldauf, R. E. Smith, U. Seljak, and R. Mandelbaum, *Phys. Rev. D* **81**, 063531 (2010), 0911.4973.
- [48] R. Ma, P. Zhang, Y. Yu, and J. Qin, *arXiv e-prints arXiv:2306.15177* (2023), 2306.15177.
- [49] M. von Wietersheim Kramsta, B. Joachimi, J. L. van den Busch, C. Heymans, H. Hildebrandt, M. Asgari, T. Tröster, S. Unruh, and A. H. Wright, *Monthly Notices of the Royal Astronomical Society* **504**, 1452–1465 (2021), URL <http://dx.doi.org/10.1093/mnras/stab1000>.
- [50] J. Elvin-Poole, N. MacCrann, S. Everett, J. Prat, E. S. Rykoff, J. De Vicente, B. Yanny, K. Herner, A. Ferté, E. D. Valentino, et al., *Monthly Notices of the Royal Astronomical Society* **523**, 3649 (2023), ISSN 0035-8711, <https://academic.oup.com/mnras/article-pdf/523/3/3649/50596748/stad1594.pdf>, URL <https://doi.org/10.1093/mnras/stad1594>.
- [51] S. Zhou, P. Zhang, and Z. Chen, *MNRAS* **523**, 5789 (2023), 2304.11540.
- [52] Planck Collaboration, N. Aghanim, Y. Akrami, M. Ashdown, J. Aumont, C. Baccigalupi, M. Ballardini, A. J. Banday, R. B. Barreiro, N. Bartolo, et al., *A&A* **641**, A6 (2020), 1807.06209.
- [53] D. N. Limber, *ApJ* **117**, 134 (1953).
- [54] A. Dey, D. J. Schlegel, D. Lang, R. Blum, K. Burleigh, X. Fan, J. R. Findlay, D. Finkbeiner, D. Herrera, S. Juneau, et al., *The Astronomical Journal* **157**, 168 (2019).
- [55] D. Lang, D. W. Hogg, and D. J. Schlegel, *The Astronomical Journal* **151**, 36 (2016).
- [56] A. Meisner, D. Lang, and D. Schlegel, *The Astronomical Journal* **154**, 161 (2017).
- [57] X. Yang, H. Xu, M. He, Y. Gu, A. Katsianis, J. Meng, F. Shi, H. Zou, Y. Zhang, C. Liu, et al., *The Astrophysical Journal* **909**, 143 (2021).
- [58] D. Lang, D. W. Hogg, and D. Mykytyn, *Astrophysics Source Code Library pp. ascl-1604* (2016).
- [59] H. Hildebrandt, T. Erben, K. Kuijken, L. van Waerbeke, C. Heymans, J. Coupon, J. Benjamin, C. Bonnett, L. Fu, H. Hoekstra, et al., *Monthly Notices of the Royal Astronomical Society* **421**, 2355 (2012).
- [60] L. Miller, C. Heymans, T. Kitching, L. Van Waerbeke, T. Erben, H. Hildebrandt, H. Hoekstra, Y. Mellier, B. Rowe, J. Coupon, et al., *Monthly Notices of the Royal Astronomical Society* **429**, 2858 (2013).
- [61] H. Hildebrandt, M. Viola, C. Heymans, S. Joudaki, K. Kuijken, C. Blake, T. Erben, B. Joachimi, D. Klaes, L. t. Miller, et al., *Monthly Notices of the Royal Astronomical Society* **465**, 1454 (2017).
- [62] R. Mandelbaum, B. Rowe, R. Armstrong, D. Bard, E. Bertin, J. Bosch, D. Boutigny, F. Courbin, W. A. Dawson, A. Donnarumma, et al., *Monthly Notices of the Royal Astronomical Society* **450**, 2963 (2015).
- [63] Euclid Collaboration, N. Martinet, T. Schrabback, H. Hoekstra, M. Tewes, R. Herbonnet, P. Schneider, B. Hernandez-Martin, A. N. Taylor, J. Brinchmann, et al., *A&A* **627**, A59 (2019), 1902.00044.
- [64] A. Phriksee, E. Jullo, M. Limousin, H. Shan, A. Finoguenov, S. Komonjinda, S. Wannawichian, and U. Sawangwit, *Monthly Notices of the Royal Astronomical Society* **491**, 1643 (2020).
- [65] H. Kong, K. J. Burleigh, A. Ross, J. Moustakas, C.-H. Chuang, J. Comparat, A. de Mattia, H. du Mas des Bourboux, K. Honscheid, S. Lin, et al., *Monthly Notices of the Royal Astronomical Society* **499**, 3943 (2020).
- [66] R. Zhou, J. A. Newman, Y.-Y. Mao, A. Meisner, J. Moustakas, A. D. Myers, A. Prakash, A. R. Zentner, D. Brooks, Y. Duan, et al., *Monthly Notices of the Royal Astronomical Society* **501**, 3309 (2021).
- [67] E. L. Wright, P. R. Eisenhardt, A. K. Mainzer, M. E. Ressler, R. M. Cutri, T. Jarrett, J. D. Kirkpatrick, D. Padgett, R. S. McMillan, M. Skrutskie, et al., *The Astronomical Journal* **140**, 1868 (2010).
- [68] E. Chaussidon, C. Yèche, N. Palanque-Delabrouille, A. de Mattia, A. D. Myers, M. Rezaie, A. J. Ross, H.-J. Seo, D. Brooks, E. Gaztañaga, et al., *Monthly Notices of the Royal Astronomical Society* **509**, 3904 (2021), ISSN 0035-8711, <https://academic.oup.com/mnras/article-pdf/509/3/3904/41446828/stab3252.pdf>, URL <https://doi.org/10.1093/mnras/stab3252>.
- [69] H. Xu, P. Zhang, H. Peng, Y. Yu, L. Zhang, J. Yao, J. Qin, Z. Sun, M. He, and X. Yang, *MNRAS* **520**, 161 (2023), 2209.03967.
- [70] W. J. Percival, A. J. Ross, A. G. Sánchez, L. Samushia, A. Burden, R. Crittenden, A. J. Cuesta, M. V. Magana, M. Manera, F. Beutler, et al., *Monthly Notices of the Royal Astronomical Society* **439**, 2531 (2014).
- [71] Y. Wang, G.-B. Zhao, C. Zhao, O. H. E. Philcox, S. Alam, A. Tamone, A. de Mattia, A. J. Ross, A. Raichoor, E. Burtin, et al., *Monthly Notices of the Royal Astronomical Society* **498**, 3470–3483 (2020), URL <http://dx.doi.org/10.1093/mnras/staa2593>.
- [72] N. E. Chisari, D. Alonso, E. Krause, C. D. Leonard, P. Bull, J. Neveu, A. Villarreal, S. Singh, T. McClintock, J. Ellison, et al., *ApJS* **242**, 2 (2019), 1812.05995.
- [73] R. E. Smith, J. A. Peacock, A. Jenkins, S. D. M. White, C. S. Frenk, F. R. Pearce, P. A. Thomas, G. Efstathiou, and H. M. P. Couchman, *MNRAS* **341**, 1311 (2003), astro-ph/0207664.
- [74] R. Takahashi, M. Sato, T. Nishimichi, A. Taruya, and M. Oguri, *ApJ* **761**, 152 (2012), 1208.2701.
- [75] A. J. Mead, J. A. Peacock, C. Heymans, S. Joudaki, and A. F. Heavens, *MNRAS* **454**, 1958 (2015), 1505.07833.
- [76] D. Nelson, A. Pillepich, V. Springel, R. Weinberger, L. Hernquist, R. Pakmor, S. Genel, P. Torrey, M. Vogelsberger, G. Kauffmann, et al., *Monthly Notices of the Royal Astronomical Society* **475**, 624 (2018).
- [77] V. Springel, R. Pakmor, A. Pillepich, R. Weinberger, D. Nelson, L. Hernquist, M. Vogelsberger, S. Genel, P. Torrey, F. Marinacci, et al., *Monthly Notices of the Royal Astronomical Society* **475**, 676 (2018).
- [78] D. Korytov, A. Hearin, E. Kovacs, P. Larsen, E. Rangel, J. Hollowed, A. J. Benson, K. Heitmann, Y.-Y. Mao, A. Bahmanyar, et al., *The Astrophysical Journal Supplement Series* **245**, 26 (2019), URL <http://dx.doi.org/10.3847/1538-4365/ab510c>.

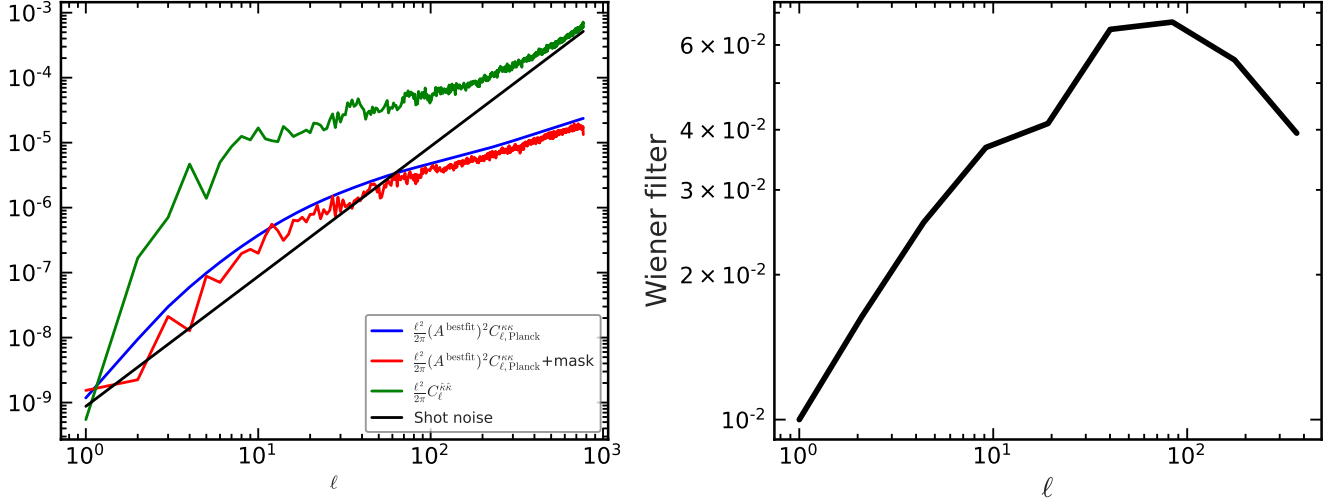


FIG. 14: Left: The angular power spectrum of the weak lensing map. The blue line is calculated from the Planck 2018 cosmology combined with the bestfit lensing amplitude A^{bestfit} , while after applying the DECaLS mask the calculation is shown with the red line. The green line is the measurement from the reconstructed convergence map. The black line represents the shot noise. Right: The associated Wiener filter calculated from the angular power spectrum.

VI. APPENDIX

A. Wiener filter

For the spherical harmonic coefficients $\hat{\kappa}_{\ell m}$ estimated by Healpix, the Wiener filter is calculated by

$$\hat{\kappa}_{\ell m}^{\text{WF}} = \frac{C_{\ell}^{\text{signal}}}{C_{\ell}^{\text{signal}} + C_{\ell}^{\text{noise}}} \hat{\kappa}_{\ell m}. \quad (30)$$

Where C_{ℓ}^{signal} is the auto power spectrum of the lensing signal and C_{ℓ}^{noise} is that of the noise. We calculate C_{ℓ}^{signal} from the Planck 2018 cosmology combined with the bestfit amplitude A^{bestfit} . To take into account the impact of survey geometry, we generate 100 full-sky maps of the power spectrum $(A^{\text{bestfit}})^2 C_{\ell, \text{Planck}}^{\kappa\kappa}$. We then apply the mask to these maps and obtain 100 power spectra with the DECaLS mask. We use the average one to get C_{ℓ}^{signal} .

We calculate $C_{\ell}^{\text{signal}} + C_{\ell}^{\text{noise}}$ by the auto power spectrum of the reconstructed lensing map $\hat{\kappa}$, which is

$$C_{\ell}^{\hat{\kappa}\hat{\kappa}} = \frac{1}{2\ell + 1} \sum_{m=-\ell}^{\ell} \hat{\kappa}_{\ell m}^* \hat{\kappa}_{\ell m}. \quad (31)$$

Take the reconstructed lensing map of the baseline set (the first row in Table III) as an example, the results of the power spectrum is shown in Fig.14. The auto power spectrum of the reconstructed lensing map is overwhelmed by the shot noise at $\ell > 50$, which agrees with the results in [48]. This is the reason why we have used the cross correlation to increase the S/N. The associated Wiener filter calculated by Eq.(30) is shown in the right panel of Fig.14 and the lensing convergence map after applying the Wiener filter is shown in Fig.7.